Natural Convection in Steady Solidification: Finite Element Analysis of a Two-Phase Rayleigh–Bénard Problem

CHIECHUN J. CHANG AND ROBERT A. BROWN

*Department of Chemical Engineering,
Massachusetts Institute of Technology, Cambridge, Massachusetts 02139*

Galerkin finite-element approximations and Newton's method for solving free boundary problems are combined with computer-implemented techniques from nonlinear perturbation analysis to study solidification problems with natural convection in the melt. The Newton method gives rapid convergence to steady state velocity, temperature and pressure fields and melt–solid interface shapes, and forms the basis for algebraic methods for detecting multiple steady flows and assessing their stability. The power of this combination is demonstrated for a two-phase Rayleigh–Bénard problem composed of melt and and solid in a vertical cylinder with the thermal boundary conditions arranged so that a static melt with a flat melt–solid interface is always a solution. Multiple cellular flows bifurcating from the static state are detected and followed as Rayleigh number is varied. Changing the boundary conditions to approach those appropriate for the vertical Bridgman solidification system causes imperfections that eliminate the static state. The flow structure in the Bridgman system is related to those for the Rayleigh–Bénard system by a continuous evolution of the boundary conditions.

1. INTRODUCTION

Buoyancy-driven convection in the melt plays an important role in setting heat and mass transfer in solidification processes for producing the precise single-crystal semiconductor materials that are the foundation of the microelectronics industry. The compositional uniformity of crystals grown by either the Czochralski or floating-zone methods for producing silicon [1] and the vertical Bridgman–Stockbarger system [2] studied here is strongly coupled to the structure of the fluid motion in the melt and to the shape of the melt–solid interface. Obtaining a quantitative understanding of the composition of crystals grown by these methods requires efficient and accurate numerical methods for the solution of solidification models including natural convection in the melt.

Even the steady state versions of these solidification problems are formidable free-boundary problems composed of conservation equations written in terms of the field variables, velocity and pressure in the melt and temperature in both phases. These equations are coupled to the location of the melt–solid interface through the two

1

interfacial conditions for the equilibrium melting temperature and the balance of heat fluxes. The convective terms in the conservation equations and the coupling between the temperature field and the location of the melt–solid interface introduce nonlinearities into the equation set. Traditional numerical schemes for free-boundary problems iterate between the calculation of the field variables for a particular interface shape and calculation of updates to the shape using either the condition for the melting point isotherm or the balance of heat flux across the phase boundary *distinguished* for this purpose.

In this paper, we present a Galerkin finite element method combined with Newton's method for calculating axisymmetric fluid flow and melt–solid interface shape in a sequence of steady solidification problems. The finite-element formulation uses the curved meshes needed for accurate approximation to the melt–solid interface shape, allows simple incorporation of heat flux boundary conditions, and seems superior to finite difference methods [3–4] for including natural convection in steady solidification problems. Several recent studies [5–7] have demonstrated the advantages of formulating Newton's methods for simultaneous solution of the Galerkin residual equations for the field variables and the interface shape. Each study shows the increase in computational efficiency due to the quadratic convergence rate of Newton's method [8] compared to the linear convergence of successive iterations. The finite element formulation and Newton's iteration are presented in Subsection 3.1.

Besides giving rapid convergence, Newton's method forms the basis for powerful computer-aided techniques [9–12] for tracking the nonlinear structure of the solutions of algebraic equations with changes in a parameter. These methods take the approach of bifurcation theory [13] and follow families of solutions while locating singular points where either two or more families have a common solution—a bifurcation point—or a single family turns around in the parameter. The presence of such singular points is also linked [11, 13] to temporal stability when the solution of the nonlinear equations represents the steady state of a set of evolution equations. In this paper, these computer-aided algorithms are applied to steady solidification problems to determine the structure of the flow and thermal fields and the shape of the melt–solid interface with changes in Rayleigh number Ra which measures the intensity of the convection. Our formulations of the algorithms for nonlinear analysis are described in detail in [11] and are briefly discussed in Subsection 3.2.

The sequence of solidification problems described in Section 2 are based on melt and solid stratified in a vertical cylindrical ampoule. The problems vary according to the thermal boundary conditions specified along the walls of the ampoule. At one limit of the sequence the thermal conditions describe a two-phase Rayleigh–Bénard problem [14]. Melt is held below (with respect to gravity) the solid and the temperature distribution along the ampoule is set so that a purely axial thermal gradient is imposed on the melt and solid. A static melt and a flat melt–solid interface satisfies the Boussinesq equations and the energy balance in the solid for all Rayleigh numbers and is analogous to the base state from which cellular flows develop in the single-phase problem of a liquid in a vertical cylinder heated from below [11, 12, 15]. The effect of the melt–solid interface on the structure of these

cellular flows is accessed by comparing the results of the single- and two-phase problems. For this, it is useful to review the flow structure for liquid in a vertical cyclinder, as discussed in [12].

In the single-phase problem, the static melt becomes unstable at a critical Rayleigh number $Ra_c^{(1)}$, and two families of axisymmetric cellular flows develop toward higher values of Ra. The flows in each of the families at the same value of Ra are identical up to a reflection about the plane perpendicular to the axis and passing through the middle of the cylinder. When the flows have only one cell in the axial direction the two flows are conveniently classified according to whether the fluid moves upward (1U) or downward (1D) along the axis of the cylinder.

Although the critical values of Rayleigh number are similar for both the melt and melt–solid systems, the evolution of the flow fields and the structure of the flow families are quite different. As is shown in Section 4.1, deformation of the melt–solid interface caused by convective heat transfer breaks the symmetry that exists in the flow field for the single-phase problem and causes differences in the structures of the two flow families that evolve from each critical value Ra_c. This loss of symmetry is an "imperfection" in the non-linear structure of the solution and ruptures a secondary bifurcation point that exists for the single-phase problem.

The remainder of the sequence of solidification problems is populated by cylindrical configurations that represent a continuous transition in the thermal boundary conditions between the Rayleigh–Bénard and the vertical Bridgman geometries [2]. These changes in the thermal conditions introduce radial temperature gradients that destroy the static state and cause fluid motion for all values of Ra; for small differences from the Rayleigh–Bénard problem and small deviations of the Rayleigh number from the critical value the structure of the flow families is described by the theory of imperfect bifurcations, as has been applied to natural convection by a
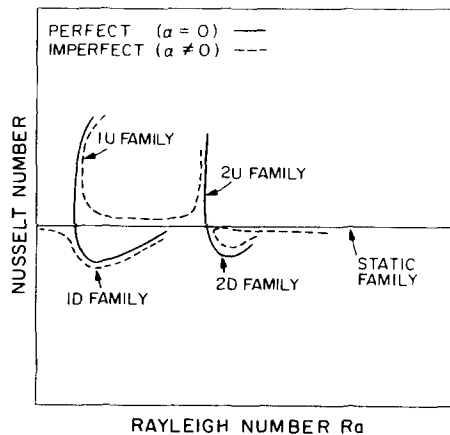

RAYLEIGH NUMBER Ra

FIG. 1. Families of axisymmetric flows emanating from the first and second bifurcation points for both perfect ($\alpha = 0$) and imperfect ($\alpha \neq 0$) boundary conditions. Family names refer to results discussed in Section 4.

number of researchers [16–19]. The changes in the thermal boundary conditions separate flow families that had joined at a bifurcation point into distinct solution curves; the rupturing of the solution families originating at the first two critical Rayleigh numbers is depicted on Fig. 1 by the dashed curves. One family evolves smoothly past the value of Ra_c while the other exists only for values of Ra greater than Ra_c and is locally multi-valued with respect to Ra. In Section 4, finite element calculations combined with techniques for analysis described in Subsection 3.2 are used to connect the structure of the solutions of the Rayleigh–Bénard problem to results for solidification problems in the sequence extending to the Bridgman geometry.

2. SEQUENCE OF MODEL TWO-PHASE PROBLEMS

The two-phase Rayleigh–Bénard problem and the steady-state prototype of the vertical Bridgman growth system studied here are mathematically embedded as the limiting cases in a sequence of two-phase natural convection problems with solid layered above the melt in a cylindrical ampoule of length L and radius R. The thermal boundary conditions for the Rayleigh–Bénard problem are shown in Fig. 2a. Here the bottom of the ampoule is set at a temperature T_H above the melting point T_m and the top is set at T_C below T_m. The sidewall of the ampoule is taken to be perfectly conducting with a linear temperature profile varying between the temperature of the bottom and top of the ampoule.

The thermal conditions for the vertical Bridgman system are shown in Fig. 2b and consist of hot and cold regions of the ampoule separated by an adiabatic or gradient
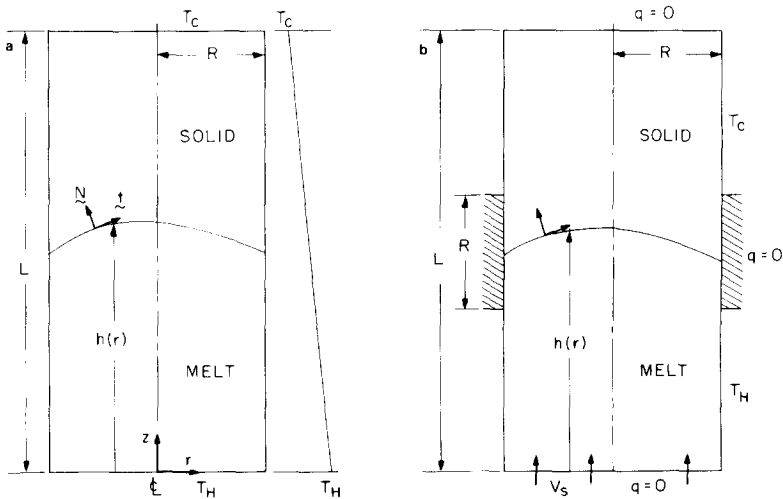

FIG. 2. Model two-phase systems; (a) Rayleigh–Bénard problem, (b) prototype of vertical Bridgman crystal growth system.

zone designed to promote steep axial temperature gradients and a planar phase boundary at the solidification front. The top and bottom of the ampoule in the Bridgman system are taken to be adiabatic. The motion of the ampoule and the growth of the crystal are modelled by uniform axial velocities through the top and bottom of the ampoule and corresponds to assuming that the ampoule extends far enough into both isothermal regions of the furnace that transients caused by the ends of the ampoule can be neglected. The growth rates in the melt U_l and solid U_s are related by the ratio of densities $d \equiv (\rho_s/\rho_l)$ as $U_l = dU_s$.

Field variables are written in terms of a cylindrical coordinate system with its origin at the bottom of the ampoule and the height L is introduced as a length scale for constructing dimensionless variables. The shape of the melt–solid interface is described by a single-valued function of the radial coordinate $z = h(r)$; then the unit vectors normal $\mathbf{N}$ and tangential $\mathbf{t}$ to this interface are

$$\mathbf{N} = (\mathbf{e}_z - h_r\mathbf{e}_r)/\sqrt{1 + h_r^2}, \qquad \mathbf{t} = (\mathbf{e}_r + h_r\mathbf{e}_z)/\sqrt{1 + h_r^2}, \tag{1}$$

where $h_r \equiv dh/dr$ and $(\mathbf{e}_r, \mathbf{e}_z)$ are unit vectors in the cylindrical coordinate system.

Steady axisymmetric convection in the melt is modelled by the Boussinesq equations [20], which are in dimensionless form

$$\nabla \cdot \mathbf{v}_l = 0, \tag{2}$$

$$\mathbf{v}_l \cdot \nabla\mathbf{v}_l = -\nabla p + \Pr \nabla^2\mathbf{v}_l + \mathrm{Ra} \, \Pr \, \theta_l\mathbf{e}_z, \tag{3}$$

$$v_l \cdot \nabla\theta_l = \nabla^2\theta_l, \tag{4}$$

where $\nabla = \mathbf{e}_r \, \partial/\partial r + \mathbf{e}_z \, \partial/\partial z$ is the gradient operator in cylindrical coordinates. The dimensionless velocities and pressure are scaled with α_l/L and $\rho_l\alpha_l^2/L^2$, respectively, where α_l is the thermal diffusivity of the melt and ρ_l is the melt density. The dimensionless melt temperature Θ_l is formed from the dimensional field $T_l(r, z)$ as $\Theta_l \equiv (T_l - T_C)/(T_H - T_C)$, where T_H and T_C are the maximum and minimum temperatures specified along the boundaries of the ampoule. The Prandtl and Rayleigh numbers are defined as $\Pr \equiv \nu/\alpha_l$ and $\mathrm{Ra} \equiv \beta g(T_H - T_C)L^3/\nu\alpha_l$, ν is the kinematic viscosity of the melt, β is the coefficient of thermal expansion, and g is the acceleration of gravity.

The dimensionless temperature is the crystal $\theta_s \equiv (T_s - T_C)/(T_H - T_C)$ is governed by the energy balance

$$\mathrm{Pe} \, \mathbf{e}_z \cdot \nabla\Theta_s \equiv \gamma\nabla^2\Theta_s, \tag{5}$$

where $\gamma \equiv \alpha_s/\alpha_l$ is the ratio of thermal diffusivities in solid and melt and $\mathrm{Pe} \equiv U_sL/\alpha_l$ is the dimensionless pull rate of the crystal. The shape of the melt–solid interface is set by the condition for the equilibrium melting point $\theta_m \equiv (T_m - T_C)/(T_H - T_C)$ and by the interfacial energy balance at the solidification boundary. These interface conditions are written in dimensionless form as

$$\theta_s = \theta_l = \theta_m, \tag{6}$$

$$\mathbf{N} \cdot \nabla\Theta_s - K\mathbf{N} \cdot \nabla\Theta_l = S \, \mathrm{Pe}(e_z \cdot \mathbf{N}), \tag{7}$$

where the contribution of latent heat is measured by the Stefan number $S \equiv \Delta H_f/c_P(T_H - T_C)$ (ΔH_f is the heat of fusion and c_p is the heat capacity of the solid) and the ratio of thermal conductivities in the melt and solid is given by $K \equiv k_l/k_s$.

The boundary conditions on velocity along the ampoule walls and the melt–solid interface are

$$v_r = 0, \qquad v_z = \text{Pe}, \qquad 0 \leqslant r \leqslant \Lambda, \qquad z = 0, \tag{8}$$

$$v_r = 0, \qquad v_z = \text{Pe}, \qquad r = \Lambda, \qquad 0 \leqslant z \leqslant h(\Lambda), \tag{9}$$

$$\mathbf{v} \cdot \mathbf{t} = \text{Pe}(\mathbf{e}_z \cdot \mathbf{t}), \qquad d(\mathbf{v} \cdot \mathbf{N}) = \text{Pe}(\mathbf{e}_z \cdot \mathbf{N}), \qquad 0 \leqslant r \leqslant \Lambda, \qquad z = h(\Lambda), \tag{10}$$

where $\Lambda \equiv R/L$ is the aspect ratio of the cylinder. Conditions (10) at the melt–solid interface ensure no slip tangential to the crystal and incorporation of melt into the crustal at a rate proportional to the growth rate.

The thermal boundary conditions for the two systems shown in Fig. 2 are incorporated mathematically into the same set by introducing the artificial parameters α and β, each ranging between zero and one. The thermal conditions at the top and bottom of the ampoule are

$$(1 - \alpha)\Theta_l + \alpha(\partial\Theta_l/\partial z) = 0, \qquad z = 0, \qquad 0 \leqslant r \leqslant \Lambda, \tag{11}$$

$$(1 - \alpha)\Theta_s + \alpha(\partial\Theta_s/\partial z) = 0, \qquad z = 1, \qquad 0 \leqslant r \leqslant \Lambda. \tag{12}$$

The mathematical combination of the boundary conditions along the sidewall ($r = \Lambda$) for the two systems is complicated by the three zones of the Bridgman furnace and the unspecified location of the melting temperature on the ampoule in the Rayleigh–Bénard problem. We simplify this problem by setting Θ_m to occur at $z = \frac{1}{2}$ in the latter system. For this case, the thermal conditions along the ampoule are divided into four sections to link the two systems:

$$\Theta_l = (1 - \beta)|1 + 2z(\Theta_m - 1)| + \beta, \qquad 0 \leqslant z \leqslant l_1, \tag{13a}$$

$$(1 - \beta)\Theta_l = (1 - \beta)|1 + 2z(\Theta_m - 1)| + \beta(\partial\Theta_l/\partial r), \qquad l_1 \leqslant z \leqslant \tfrac{1}{2}, \tag{13b}$$

$$(1 - \beta)\Theta = (1 - \beta)|\Theta_m - 2\Theta_m(z - \tfrac{1}{2})|, \qquad \tfrac{1}{2} \leqslant z \leqslant (l_1 + l_2), \tag{13c}$$

$$\Theta_s = (1 - \beta)|\Theta_m - 2\Theta_m(z - \tfrac{1}{2})|, \qquad (l_1 + l_2) \leqslant z \leqslant 1, \tag{13d}$$

where $l_1 \equiv \tilde{l}_1/L$ and $l_2 \equiv \tilde{l}_2/L$ are the dimensionless lengths of the hot and adiabatic zones of the Bridgman furnace shown in Fig. 2b.

The Rayleigh–Bénard problem is recovered from Eqs. (2)–(13) by setting the parameters (Pe, α, β) equal to zero. For all values of Rayleigh number, the equation set then has the static solution

$$\mathbf{v} = \mathbf{0}, \qquad p(r, z) = p_0 + \text{Ra Pr}(z - z^2/2),$$
$$\Theta_l(r, z) = 1 + 2z(\Theta_m - 1), \qquad \Theta_s(r, z) = \Theta_m - 2\Theta_m(z - \tfrac{1}{2}), \tag{14}$$

where p_0 is an arbitrary reference pressure. To obtain this solution the ratio of thermal conductivities must be specified according to the relationship $K = \Theta_m/(1 - \Theta_m)$; then setting Θ_m close to one corresponds to a system where the conductivity of the melt is much higher than that of the solid.

Cellular flows that deform the temperature fields and the melt–solid interface bifurcate from the static state at critical values of Rayleigh number determined as a function of Θ_m. Any change in the parameters (Pe, α, β) causes the purely axial temperature fields for either the static or uniformly translating (Pe $\neq 0$) melt and solid to no longer match the temperature profiles imposed along the sidewall of the ampoule. Radial temperature gradients in the melt result and drive thermal convection for any nonzero value of Ra. Thus the parameters (Pe, α, β) cause imperfections in the Rayleigh–Bénard problem and rupture the junctions between the static and flow families that exist when Pe $= \alpha = \beta = 0$. The imperfection caused by varying α is demonstrated in Subsection 4.2.

The thermal boundary conditions for the Bridgman growth system are recovered from Eqs. (11)–(13) by setting $\alpha = \beta = 1$. The flow structures and the shapes of the melt–solid interface calculated in this configuration are attainable by a *continuous* transition from the Rayleigh–Bénard problem; this link is established in Subsection 4.3.

3. NUMERICAL METHODS

3.1. *Finite Element Analysis: The Isotherm–Newton Algorithm*

The steady solidification problem defined by Eqs. (2)–(13) is reduced to a finite-dimensional set of residual equations by representing velocities, pressure, temperature, and the shape of the melt–solid interface in expansions of finite-element basis functions. For an approximate shape of the phase boundary, both melt and solid are divided into quadrilateral elements and the field variables are approximated by mixed interpolation with finite-element bases using techniques that are well established for natural convection in confined geometries [21, 22]. The velocities in the melt and the temperature fields in both phases are approximated by expansions of Lagrangian biquadratic polynomials $\{\Phi^i(r, z)\}$

$$\begin{bmatrix} v_r(r, z) \\ v_z(r, z) \\ \Theta_l(r, z) \end{bmatrix} = \sum_{i=1}^{N_l} \begin{bmatrix} u_i \\ v_i \\ \Theta_i^{(l)} \end{bmatrix} \Phi^i(r, z), \qquad \Theta_s(r, z) = \sum_{i=1}^{N_s} \theta_i^{(s)} \Phi^i(r, r), \qquad (15)$$

where N_l and N_s are the total numbers of biquadratic functions in melt and solid. The pressure in the melt is approximated by an expansion in a basis of continuous bilinear polynomials $\{\Psi^i(r, z)\}$ as

$$p(r, z) = \sum_{i=1}^{M} P_i \Psi^i(r, z), \qquad (16)$$

where M is the number of vertex nodes in the discretization of the melt.

The shape of the melt–solid interface is approximated by a N_I-dimensional set of Hermite cubic polynomials $\Gamma^i(r)$ as

$$h(r) = \sum_{i=1}^{N_I} \beta_i \Gamma^i(r), \tag{17}$$

constructed so that the derivative of the function $h(r)$ is everywhere continuous. The number and spacing of the Hermite elements along the interface is the same as for the n_r radial elements in the discretization of melt and solid. Details of the finite-element bases are found in texts [23, 24] and in [25].

For an approximate interface shape, the weak forms of the field equations are formed by applying Galerkin's method to Eqs. (2)–(5) is the normal way for natural convection [24, 22]. The final form of the equation set is reached by applying the divergence theorem to eliminate second-derivatives and by incorporating the boundary conditions on temperature and velocity along the ampoule wall, along with the interfacial energy balance (7) and by forcing the temperature field to be continuous across the interface. The nonlinear set of algebraic equations resulting from this discretization of the field equations is written out in [25] and is represented here as

$$\mathbf{R}^{(F)}(\boldsymbol{\alpha}, \boldsymbol{\beta}; \text{Ra}, \text{Pr}) = \mathbf{0}, \tag{18}$$

where $\boldsymbol{\alpha}$ is the vector of unknown coefficients associated with the field variables and $\boldsymbol{\beta}$ is the vector of coefficients in the expansion for the interface shape. The coefficients $\{\beta_i\}$ do not enter explicitly into the integrands of the Galerkin integrals, but are involved in setting the shapes of melt and solid in the limits of these integrals. The finite-element basis functions ($\Phi^i(r, z)$, $\Psi^i(r, z)$) are also influenced by the coefficients $\{\beta_i\}$ through the shapes of the elements in the mesh.

As suggested in [5], the isotherm condition Eq. (6) is *distinguished* for calculating the shape of the melt–solid interface. Equation (6) is put in discrete form by applying Galerkin's method as

$$R_i^{(I)}(\boldsymbol{\alpha}, \boldsymbol{\beta}) = \int_0^\Lambda \Gamma^i(r)[\Theta_I(r, h(r)) - \Theta_m] \sqrt{1 + h_r^2}\, dr, \tag{19}$$

where $i = 1, \ldots, N_I$. The complete set of algebraic equations for the field variables and interface shape is now

$$\mathbf{R}(\mathbf{x}; \text{Ra}, \text{Pr}) = \begin{bmatrix} \mathbf{R}^{(F)}(\boldsymbol{\alpha}, \boldsymbol{\beta}; \text{Ra}, \text{Pr}) \\ \mathbf{R}^{(I)}(\boldsymbol{\alpha}, \boldsymbol{\beta}) \end{bmatrix} = 0, \tag{20}$$

where $\mathbf{x}^T = (\boldsymbol{\alpha}^T, \boldsymbol{\beta}^T)$.

Solution of Eqs. (20) by Newton's method requires calculation of the Jacobian matrix

$$\mathbf{J} \equiv \begin{bmatrix} \mathbf{J}^{(F)} & \mathbf{J}^{(F)} \\ \mathbf{J}^{(I)} & \mathbf{J}^{(I)} \end{bmatrix} \tag{21}$$

at each iteration, where the submatrices have components

$$\hat{J}_{ij}^{(F)} \equiv \frac{\partial R_i^{(F)}}{\partial \alpha_j}, \qquad \hat{J}_{ij}^{(I)} \equiv \frac{\partial R_i^{(I)}}{\partial \alpha_j}, \tag{22a}$$

$$\tilde{J}_{ij}^{(F)} \equiv \frac{\partial R_i^{(F)}}{\partial \beta_j}, \qquad \tilde{J}_{ij}^{(I)} \equiv \frac{\partial R_i^{(I)}}{\partial \beta_j}. \tag{22b}$$

The coefficients in the matrices $\hat{\mathbf{J}}^{(F)}$ and $\hat{\mathbf{J}}^{(I)}$ give the sensitivity of the residual equations to changes in the field variables and are evaluated by differentiating the residual equations. The two matrices $\tilde{\mathbf{J}}^{(F)}$ and $\tilde{\mathbf{J}}^{(I)}$ measure the sensitivity of the residual equations to changes in the location of the melt–solid interface and so include the changes in the basis functions caused by moving the elements. Ettouney and Brown [5] map the entire free-boundary problem to regions with fixed boundaries and a fixed finite-element mesh, so that these coefficients can be computed explicitly. Instead of this global mapping technique, we use the method proposed by Saito and Scriven [7] and take advantage of the isoparametric mapping for each quadrilateral element in (r, z) coordinates onto a square element where the dependence of the basis functions on the coefficients $\{\beta_i\}$ is expressed explicitly. This method was first applied in [6] to a steady solidification problem with natural convection and details are available in [25].

The approximations in the field variables and melt–solid interface shape are updated at each Newton iteration according to the formula

$$\begin{bmatrix} \alpha^{(k+1)} \\ \beta^{(k+1)} \end{bmatrix} = \begin{bmatrix} \alpha^{(k)} \\ \beta^{(k)} \end{bmatrix} + \delta^{(k+1)}. \tag{23}$$

where the correction vector $\delta^{(k+1)}$ is calculated as the solution of the linear equation set

$$\mathbf{J}(\mathbf{x}^{(k)})\,\delta^{(k+1)} = -\mathbf{R}(\mathbf{x}^{(k)}; \mathrm{Ra}, \mathrm{Pr}), \tag{24}$$

where $\mathbf{x}^{(k)\mathrm{T}} \equiv (\alpha^{(k)}, \beta^{(k)})^{\mathrm{T}}$. The equation set (24) is solved by Gaussian elimination using the frontal method of Hood [26]. The quadratic convergence with iteration of the Isotherm–Newton method gave a factor of three in computational efficiency over a more standard successive approximation technique based on cycling between the calculation of the field variables, by solving Eqs. (18), and the calculation of the interface shape from the isotherm condition Eq. (6).

The stream function for each flow computed by the Isotherm–Newton method is calculated by solving the linear equation

$$\frac{1}{r}\frac{\partial^2 \psi}{\partial r^2} - \frac{1}{r^2}\frac{\partial \psi}{\partial r} + \frac{1}{r}\frac{\partial^2 \psi}{\partial z^2} = \frac{\partial v_r}{\partial z} - \frac{\partial v_z}{\partial r}, \tag{25}$$

using the Galerkin finite-element method with $\psi(r, z)$ represented in a biquadratic basis. Streamlines are plotted as contours of $\psi(r, z)$.

3.2. *Analysis of Nonlinear Algebraic Equations*

Families of flow fields and melt–solid interface shapes are calculated by solution of Eq. (20) by Newton's iteration with the first approximation generated by analytic continuation methods. For the Rayleigh number $Ra = Ra^0 + \triangle Ra$, continuation methods [9, 10] give the linear approximation to the desired solution $(\alpha(Ra), \beta(Ra))$ in terms of the known solution $(\alpha(Ra^0), \beta(Ra^0))$ as

$$\begin{bmatrix} \alpha^{(0)}(Ra^0 + \triangle Ra) \\ \beta^{(0)}(Ra^0 + \triangle Ra) \end{bmatrix} = \begin{bmatrix} \alpha(Ra^0) \\ \beta(Ra^0) \end{bmatrix} + \begin{bmatrix} \alpha_{Ra} \\ \beta_{Ra} \end{bmatrix} \triangle Ra, \tag{26}$$

where the tangent vectors $\alpha_{Ra} \equiv (\partial \alpha / \partial Ra)_{Ra^0}$ and $\beta_{Ra} \equiv (\partial \beta / \partial Ra)_{Ra^0}$ are calculated from

$$\mathbf{J}(\alpha(Ra^0), \beta(Ra^0)) \begin{bmatrix} \alpha_{Ra} \\ \beta_{Ra} \end{bmatrix} = -\left(\frac{\partial \mathbf{R}}{\partial Ra} \right)_{Ra^0}, \tag{27}$$

by performing a back-substitution using the factorization of the Jacobian matrix evaluated at the converged solution for $Ra = Ra^0$.

As discussed in several references [9–11], Newton's method with continuation fails when either a bifurcation or limit point is encountered. At a bifurcation point the tangent vectors are nonunique and the Jacobian matrix is singular. Simple singularities (the only case considered here) are systematically detected by monitoring the sign of the determinant of $\mathbf{J}$ as Ra is varied; precise values for the critical points $\{Ra_c^{(i)}\}$ are determined by applying bisection in Ra. Limit points correspond to values of Ra where a family of solutions to Eq. (20) reverses direction in Ra and mark a breakdown in the parameterization in terms of Ra; this breakdown is manifested in a singular Jacobian matrix and an undefined tangent vector. We alleviate the difficulty at limit points by using a pseudo-arclength parameter s for specifying a solution instead of Ra [9, 27]. To do this, we introduce the additional residual equation

$$R_{N_t+1} \equiv (s - s_0)^2 + \|\mathbf{x}(s) - \mathbf{x}(s_0)\|_2^2 + |Ra(s) - Ra(s_0)|^2, \tag{28}$$

for defining $Ra = Ra(s)$, where $\|\mathbf{x}\|_2$ is the R_2 norm of $\mathbf{x}$, i.e., $\|\mathbf{x}\|_2^2 = \sum_{i=1}^{N_t} x_i^2$ and $(\mathbf{x}(s_0), Ra(s_0))$ is a known solution. Newton's method and continuation methods are used for solving the augmented set Eqs. (20) and (28) and follow directly from the presentation above. The $(N_t + 1)$-dimensional Jacobian matrix is nonsingular at limit points [9].

The augmented Jacobian matrix formed from Eqs. (20) and (28) is singular at bifurcation points. At a bifurcation point along a family of solutions $\mathbf{x}_0(Ra)$ a null vector $\mathbf{y}$ exists that satisfies

$$\mathbf{J}(\mathbf{x}_0(Ra_c))\mathbf{y} = \mathbf{0}. \tag{29}$$

As discussed elsewhere [9, 11], this vector describes the finite-element approximation

to the eigenfunction and gives an approximation to the new bifurcating soluion x(Ra) as

$$\mathbf{x}(\mathrm{Ra}) = \mathbf{x}_0(\mathrm{Ra}_c) + \varepsilon \mathbf{y}, \tag{30}$$

where ε is an amplitude factor, whose magnitude depends on the distance between Ra and Ra_c. The null vector $\mathbf{y}$ is calculated by one iteration of inverse iteration for a zero eigenvalue and is scaled so that $\|\mathbf{v}\|_2 = 1$. The Newton iterations are coaxed into jumping from a base to a bifurcating flow family by using Eq. (30) as an initial approximation and adjusting ε to be large enough that the iterations do not converge back to the original solution. More reliable and complicated schemes for jumping between solution families have been developed [9, 28], but were not found to be necessary for these calculations.

The presence of critical values of Ra in the form of simple bifurcation and limit points signals changes in the linear stability of steady flow fields and interface shapes found by solving Eq. (20). To see this we consider the form of the transient equations that would result from a finite element discretization of the full unsteady problem. If the coefficients $\{u_i, v_i, p_i, \Theta_i^{(l)}, \Theta_i^{(s)}, h_i\}$ in the expansions (15)–(17) are taken to be time dependent, the transient field equations and boundary conditions can be reduced to the set of nonlinear ordinary differential equations

$$\mathbf{M}(\mathbf{x}) \frac{dx}{dt} = \mathbf{R}(\mathbf{x}; \mathrm{Ra}), \tag{31}$$

where $\mathbf{M}(\mathbf{x})$ is the finite-element mass matrix [23] that depends on $\mathbf{x}(t)$ through the presence of the interface shape in the limits of the Galerkin integrals. Stability of the steady state $\mathbf{x} = \mathbf{x}_0$ to small amplitude disturbances $\hat{x}e^{\sigma t}$ is determined by substituting $\mathbf{x} = \mathbf{x}_0 + \hat{x}e^{\sigma t}$ into Eq. (31) and collecting terms that are linear in $\hat{x}$; this yields

$$\sigma \mathbf{M}(\mathbf{x}_0)\hat{\mathbf{x}} = \mathbf{J}(\mathbf{x}_0)\hat{\mathbf{x}}, \tag{32}$$

where $\mathbf{J}(\mathbf{x}_0)$ is the Jacobian matrix evaluated about the steady-state solution. Clearly, a simple singular point in $\mathbf{J}(\mathbf{x}_0)$ corresponds to the vanishing of a real eigenvalue σ and marks the exchange of stability of the solution $\mathbf{x}_0$ xith respect to the disturbance with spacial structure $\hat{x}$. Then a stable flow must become unstable at either a simple bifurcation or limit point. We will use this criterion to determine the stability of flows to axisymmetric, temporally monotonic perturbations. Perturbations that have a time-periodic component lead to complex eigenvalues σ; zero real components of these eigenvalues correspond to the bifurcation of time-periodic flows, so-called Hopf bifurcations [13], and have been detected in other natural convection problems by calculation of the eigenvalues [29].

4. NUMERICAL RESULTS

The Isotherm–Newton method was used in conjunction with the techniques for nonlinear analysis described in the last section to study three two-phase problems from the sequence presented in Section 2. Besides, the limiting cases of the Rayleigh–Bénard (Pe $= \alpha = \beta = 0$) and the Bridgman configuration ($\alpha = \beta = 1$), results for the intermediate configuration of an ampoule with imperfect thermal conditions ($\alpha = 1$, $\beta = $ Pe $= 0$) are also presented. In each case, the aspect ratio is $\Lambda = 0.25$, $\gamma = d = K = 1.0$ and the dimensionless melting point $\Theta_m = 0.5$. The calculations presented in Subsections 4.1–4.3 are for a melt with a Prandtl number of unity. Extensive studies of numerical accuracy presented in |6| demonstrated that the flow and thermal fields and interface shapes for this set of parameters are well approximated by a uniform mesh of four radial and eight axial elements in each phase, a total of 64 elements and 658 unknowns. This mesh was used in all calculations in these subsections.

4.1. The Rayleigh–Bénard Problem: $\alpha = \beta = $ Pe $= 0$

The bifurcation points $\{ \mathrm{Ra}_c^{(i)} \}$ between the static solution Eq. (14) and solutions composed of steady cellular flows were located using the determinant of the Jacobian
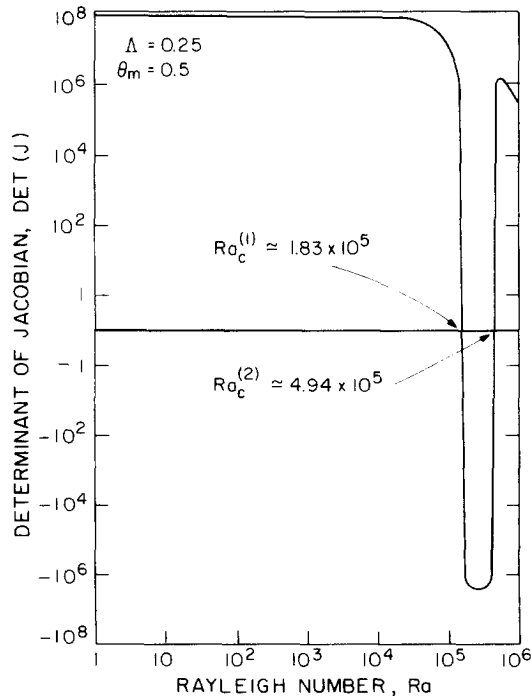

FIG. 3. Determinant of the Jacobian matrix evaluated about the static solution Eq. (14) as a function of Rayleigh number for $\Theta_m = \frac{1}{2}$.

matrix evaluated about the solution Eq. (14), which is plotted as a function of Rayleigh number on Fig. 3. The lowest two critical values were calculated as $Ra_c^{(1)} \simeq 1.83 \times 10^5$ and $Ra_c^{(2)} \simeq 4.94 \times 10^5$. The forms of the field variables and interface shapes in the bifurcating families were recovered by calculating the null vectors of the Jacobian matrix at the bifurcations points. Flows in the two families emanating from the value $Ra = Ra_c^{(1)}$ were composed of a single axisymmetric cell with melt moving either upward (1U family) or downward (1D family) at the centerline of the ampoule. The flows originating at the second critical value $Ra_c^{(2)}$ had two cells stacked axially and were divided into the 2U and 2D families depending on whether the motion in the top cell was up or down along the centerline. The stream function and temperature fields corresponding to flows in each family close to the bifurcation points are shown as the first plots in Figs. 5–8. In each case, the temperature field and melt–solid interface shape were not noticeably perturbed from the one-dimensional field and flat interface of the static solution Eq. (14).

The critical values $Ra_c^{(i)}$ for the two-phase problem were compared directly to values for a liquid in a cylindrical ampoule twice as long as its radius and with a perfectly conducting sidewall. The values of $Ra_c^{(1)}$ and $Ra_c^{(2)}$ calculated with the same finite-element approximation to the Boussinesq equations used here but applied to the single-phase system (see [12] for details) are 1.88×10^5 and 5.12×10^5, respectively;

described above. Comparing the critical values for the single- and two-phase systems suggests that the presence of the melt–solid interface has only a slight destabilizing effect on the static. melt. This slight difference in the critical Rayleigh numbers is caused by the freedom of the interface to deform. Increasing the conductivity of the solid ($K \gg 1$) so that its temperature is almost uniform increases the critical value $Ra_c^{(1)}$ to a limiting value still below the value for the single-phase system. Even in this extreme case, the melt–solid interface may still deform.

The differences in the flows caused by the melt–solid interface are more pronounced away from the critical values. The structures of the flows and interface shapes that evolve with increasing Rayleigh number from the two values $(Ra_c^{(1)}, Ra_c^{(2)})$ were calculated by the scheme outlined in Section 3. These solutions are represented in Fig. 4 by the dimensionless Nusselt number at the melt–solid interface for each flow

$$Nu_l \equiv \int_0^\Lambda \mathbf{N} \cdot \nabla\Theta_l \sqrt{1 + h_r^2}\, r\, dr, \qquad (33)$$

plotted against Ra. Samples of the temperature and flow fields in each family are shown in Figs. 5–8.

The first major difference between the one- and two-phase systems becomes apparent by examining the evolution of the 1D and 1U families. The presence of the melt–solid interface causes the structure of the flows in these families to differ, contrary to the families in the single-phase problem where the 1D and 1U flows are identical up to a reflection of the velocity field, as described in Section 1. For the 1U
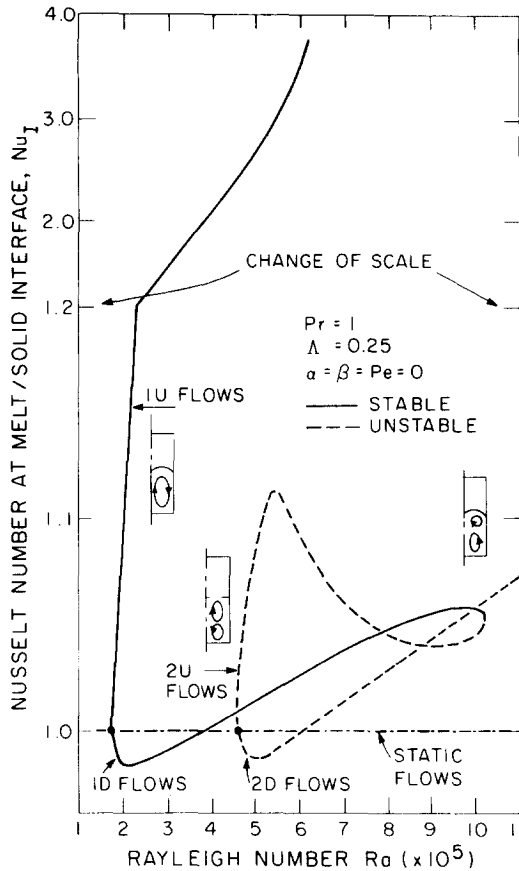
FIG. 4.   Families of axisymmetric steady states for the Rayleigh–Bénard problem.

family of the melt–solid system, hot melt moved upward along the centerline of the ampoule and pushed the phase boundary substantially higher into the ampoule with increasing Ra; melt–solid interface shapes for members of this family are shown in Fig. 6. The single cell deformed continuously with the melt–solid interface until calculations were terminated at $Ra = 6.0 \times 10^5$ because the mesh no longer resolved adequately the shape of the melt–solid interface. Up to this value of Ra, no secondary flow cells were observed.

For flows in the 1D family, hot melt rising along the wall impacted the melt–solid interface at its junction with the ampoule, as shown in Fig. 5. The linear temperature profile specified along the wall on the ampoule pinned the location of the phase boundary at $z = \frac{1}{2}$ and damped the deformation of the interface with increasing Ra. For Rayleigh numbers greater than 6×10^5, a toroidal vortex formed in the upper corner of the melt and directed the hot fluid more toward the center of the interface.
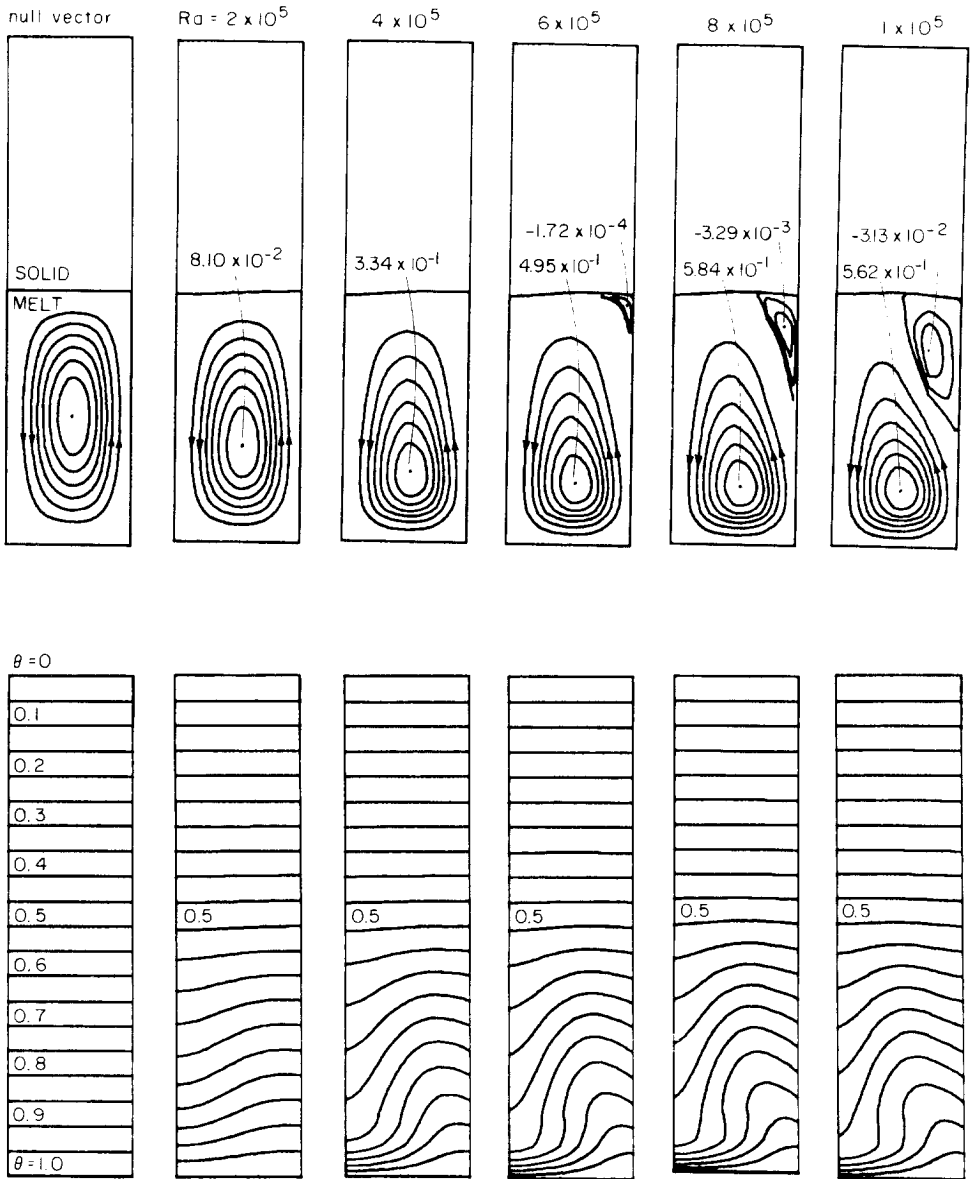
null vector   Ra = 2 x 10⁵   4 x 10⁵   6 x 10⁵   8 x 10⁵   1 x 10⁵

FIG. 5. Representative streamlines and isotherms for flows in the 1D family.

null vector   Ra = 2 x 10^5 3 x 10^5 4 x 10^5 5 x 10^5 6 x 10^5

SOLID

MELT

$\Psi = -9.35 \times 10^{-2}$

-2.63×10^{-1}

-4.09×10^{-1}

-5.39×10^{-1}

-6.60×10^{-1}

$\theta = 0$

0.1

0.2

0.3

0.4

0.5

0.5

0.5

0.5

0.5

0.5

0.6

0.7

0.8

0.9

$\theta = 1.0$
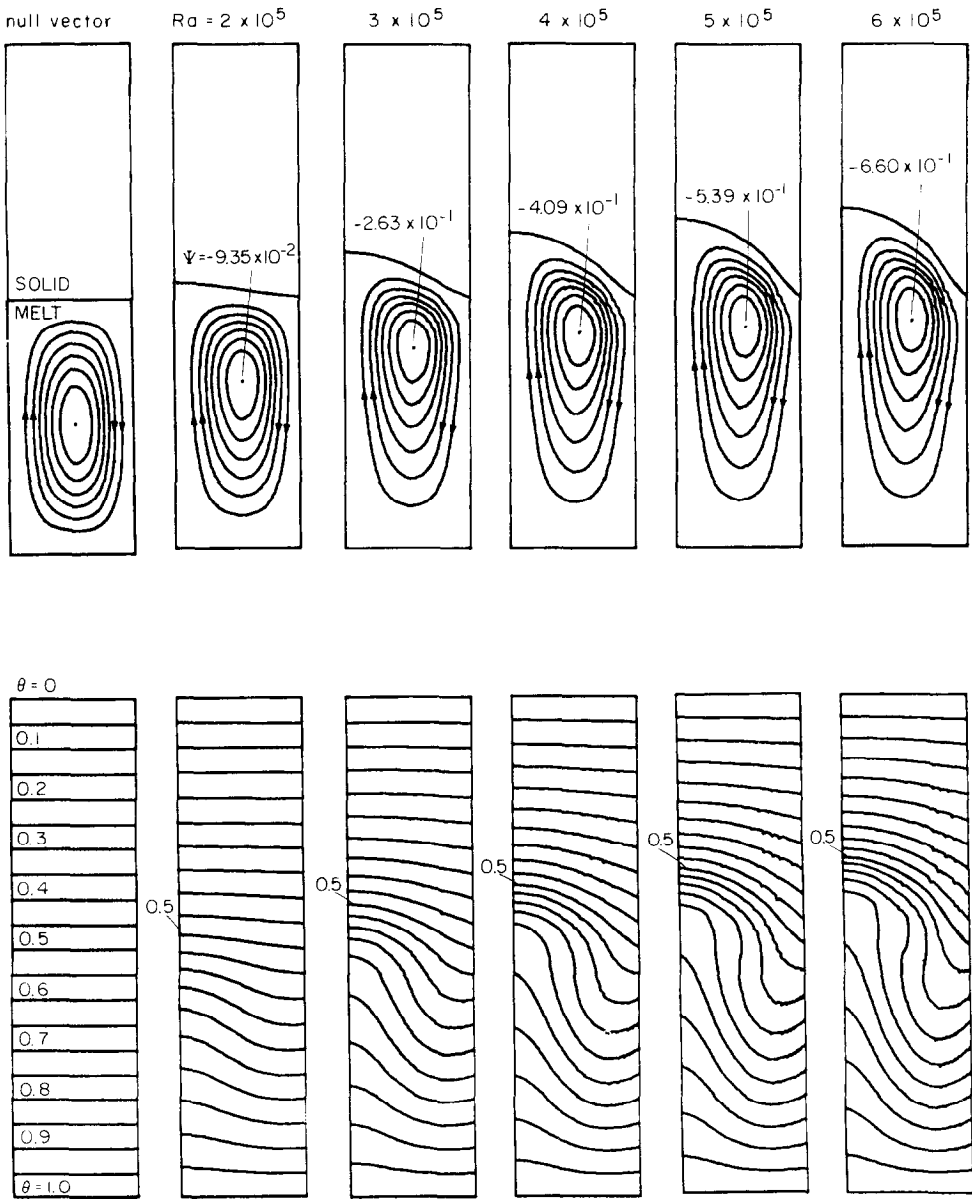
FIG. 6.   Representative streamlines and isotherms for flows in the 1U family.
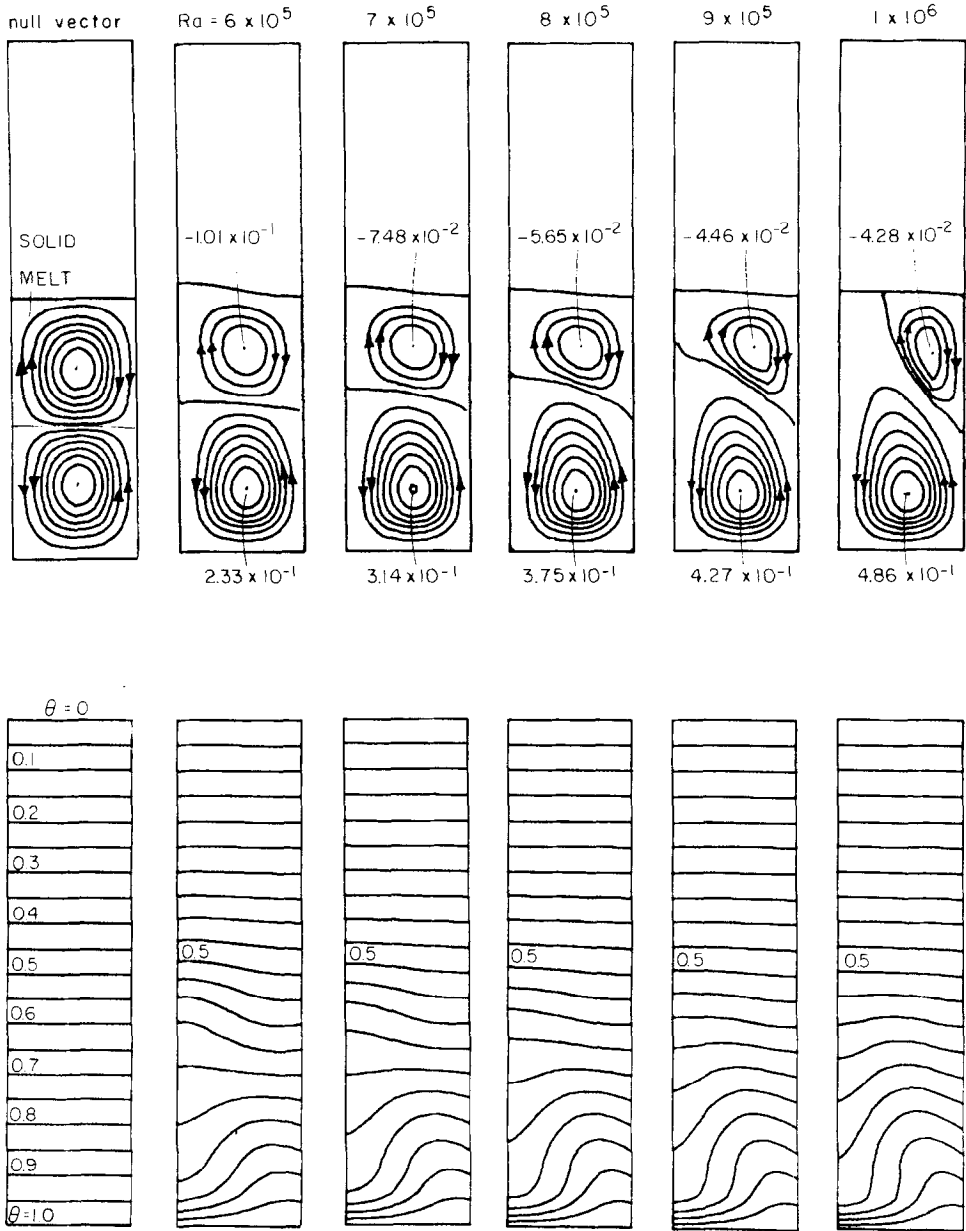
FIG. 7. Representative streamlines and isotherms for flows in the 2U family.
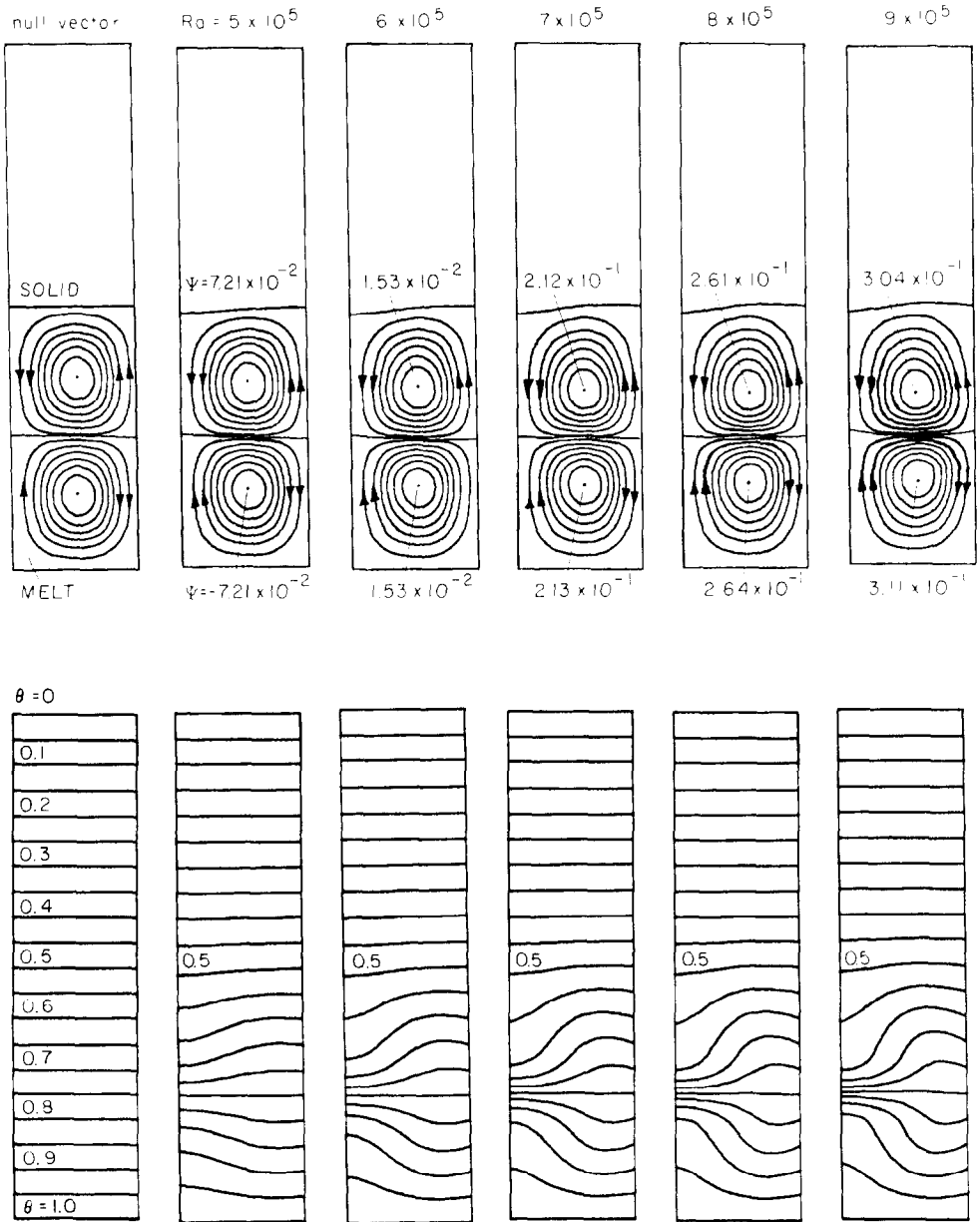
FIG. 8.   Representative streamlines and isotherms for flows in the 2D family.

The distortion of the phase boundary caused by this change in the flow field is shown by the sample interface shapes in Fig. 9.

Flows and interface shapes in the 1D family were only found for Rayleigh numbers less than $Ra = Ra_l \simeq 1.1 \times 10^6$, where the flow family turned back to lower values of Ra. The flows near this limit point in Ra are distinguished by a weakening

Flows in the 1D family beyond the limiting value Ra_l connect with flows in the 2U flow family to form a continuous curve of steady solutions, as depicted in Fig. 4. Originating from $Ra = Ra_c^{(2)}$ with two cells of the same size, both cells in the 2U flows intensified with small increases in Ra and the Nusselt number increased. As shown on Fig. 7, the top cell weakened and the bottom cell dominated the flow for Rayleigh numbers greater than 6×10^5; the Nusselt number decreased as the circulation in the top cell became so weak relative to the bottom one that it shielded the melt–solid interface from the intense convection. At higher Rayleigh numbers the bottom cell pushed the top cell to the ampoule wall and the flow fields and interface shapes in the 2U family evolved to the same form as the solutions in the 1D family. These two families join at the limit point.
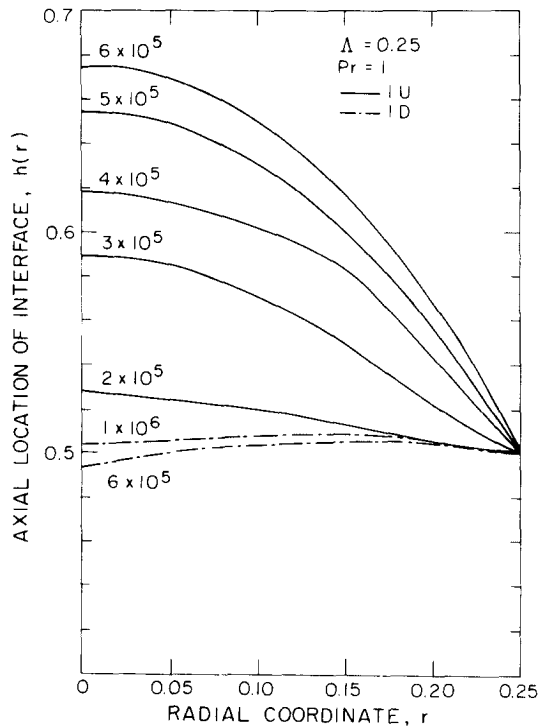

FIG. 9. Melt–solid interface shapes for flows in the 1U and 1D families for several values of Rayleigh number.

Flows in the 2D family evolved from the bifurcation point $Ra_c^{(2)}$ towards higher values of Rayleigh number. Both cells intensified equally and the melt–solid interface was little deformed, as shown by the sample streamlines in Fig. 8. The stability of the flows represented on Fig. 4 to axisymmetric, temporally monotonic perturbations of the field variables and interface shape is assessed simply by examining the connectivity of the families. The static state is stable at zero Rayleigh number and loses stability at $Ra_c^{(1)}$, where a single real eigenvalue σ_1 crosses zero and becomes positive. The flows in the 1U and 1D families that originate from $Ra_c^{(1)}$ are stable; i.e., all the real eigenvalues are negative. The steady states in the 1D family lose stability at the limit point $Ra = Ra_l$, where the 1D family joins the 2U family. Conversely, the flows in the 2U family are unstable beyond $Ra_c^{(2)}$ to a single perturbation, but regain stability at Ra_l. Flows in the 2D family are unstable to a single perturbation for the range of Rayleigh number studied here.

4.2. Imperfect Rayleigh–Bénard Problem: $\alpha = 1, \beta = Pe = 0$

Forcing the ends of the ampoule to be adiabatic created radial temperature gradients that drove convective flows for all values of Ra. The family of flows and interface shapes calculated for $Pr = 1$ and $\beta = Pe = 0$ are represented in Fig. 10; isotherms and streamlines for sample solutions along this family are shown in Fig. 11. At low Rayleigh numbers, the flows were composed of a single cell with hot melt rising along the wall of the ampoule and resembled fluid motions in the 1D family for $\alpha = 0$; see Fig. 11a. At higher values of Ra, a second cell developed in the upper corner of the ampoule and intensified with increasing Ra, as shown by Fig. 11b. The family of solutions reached a limit point at $Ra = Ra_l^{(1)} \simeq 1.16 \times 10^6$ and turned back to lower values of Ra.

The structure of the solution family for the imperfect configuration ($\alpha = 1$) up to and beyond $Ra = Ra_l^{(1)}$ can be predicted qualitatively by examining the effect of the imperfection on the solution families present for $\alpha = 0$. Making the ends of the ampoule adiabatic ruptured the bifurcation points and cause fluid flow for all members of what was the static family. As shown on Fig. 1, the solutions to the imperfect problem for values of Ra less than $Ra_l^{(1)}$ are composed of the static and 1D families of the perfect problem which combine smoothly when α is not equal to zero. The 1U family of flows couple with the reminants of the static family beyond the original critical point $Ra_c^{(1)}$ to form a continuous curve of solutions with a limit point.

The limit point $Ra_l^{(1)}$ located in the solution family for the imperfect Rayleigh–Bénard problem was analogous to the limit point Ra_l that existed in the 1D family for $\alpha = 0$. In flows along the subcritical solution branch for Ra less than $Ra_l^{(1)}$, the second cell continued to intensify and spread over the top of the melt until the patterns of streamlines qualitatively resembled flows belonging to the 2U family; see Fig. 11c. This resemblence was expected from the connection of the 1D and 2U flow families for the perfect problem ($\alpha = 0$) at the limit point Ra_l and the fact that limit points are unaltered by imperfections [13].

The flow family in the imperfect problem turned back toward higher values of Rayleigh number at $Ra = Ra_l^{(2)} \simeq 7.11 \times 10^5$. A sample flow along this new super-
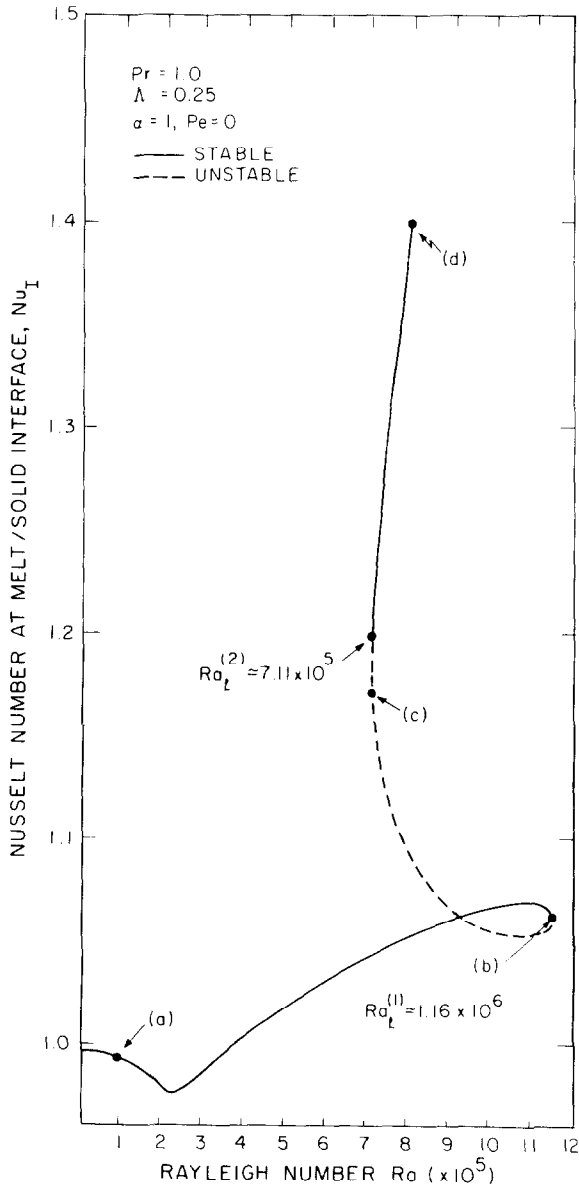
FIG. 10. Families of axisymmetric steady states for the imperfect Rayleigh–Bénard problem with $\alpha = 1$, $\beta = Pe = 0$, $Pr = 1$, θ and $\Lambda = 0.25$. Each flow field is represented by the Nusselt number at the melt–solid interface. Letters refer to sample isotherms and streamlines plotted in Fig. 11.
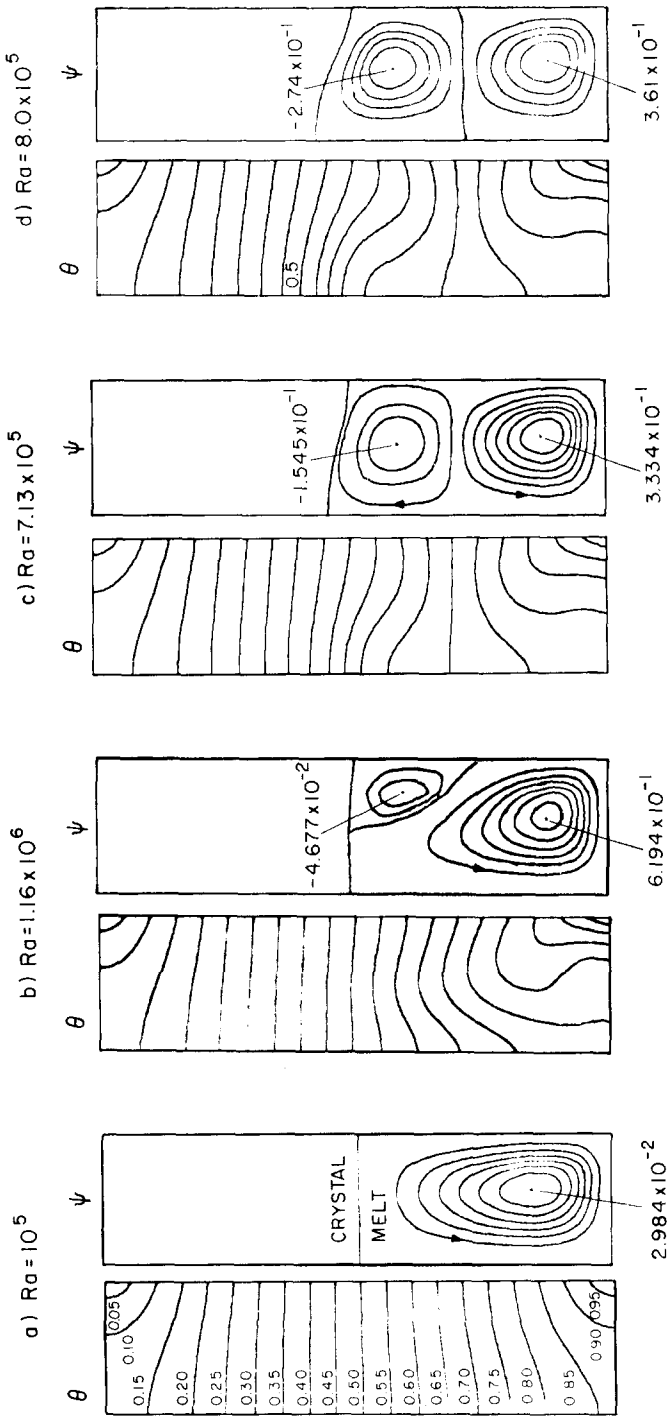
FIG. 11. Representative streamlines and isotherms for melt–solid system with $\alpha = 1$, $\beta = Pe = 0$, $Pr = 1$, and $\Lambda = 0.25$. Letters refer to points in Fig. 10.

critical branch is displayed as Fig. 11d. Here, the upper cell was more intense than the lower one, which was forced toward the bottom of the ampoule, and resembled a flow in the 1U family for $\alpha = 0$ with the lower cell positioned to account for the radial gradient introduced by the imperfection. The existence of the second supercritical solution branch for $\alpha = 1$ and its similarities with flows in the 1U family were expected because of the connectivity of the 1D and 2U families for $\alpha = 0$ and because the 1U family evolved supercritically with respect to Rayleigh number. The limit point $Ra_l^{(2)}$ calculated for $\alpha = 1$ is precisely the limit point proposed in Fig. 1 for separating the 1U and static flow families in a slightly imperfect ($\alpha \ll 1$) system.

The stability of each flow for $\alpha = 1$, as indicated in Fig. 11d, was reasoned from the stability of the flows for the perfect Rayleigh–Bénard problem and the evolution of the flows with changes in α. Both the initial branch of the solution family evolving from zero Ra up to the limit point $Ra_l^{(1)}$ and the second supercritical branch that exists for Rayleigh numbers greater than $Ra_l^{(2)}$ are stable to temporally monotonic and spatially axisymmetric disturbances. For Rayleigh numbers in the range $7.11 \times 10^5 \leqslant Ra \leqslant 1.16 \times 10^6$ both branches contain solutions and two stable steady solutions are possible.
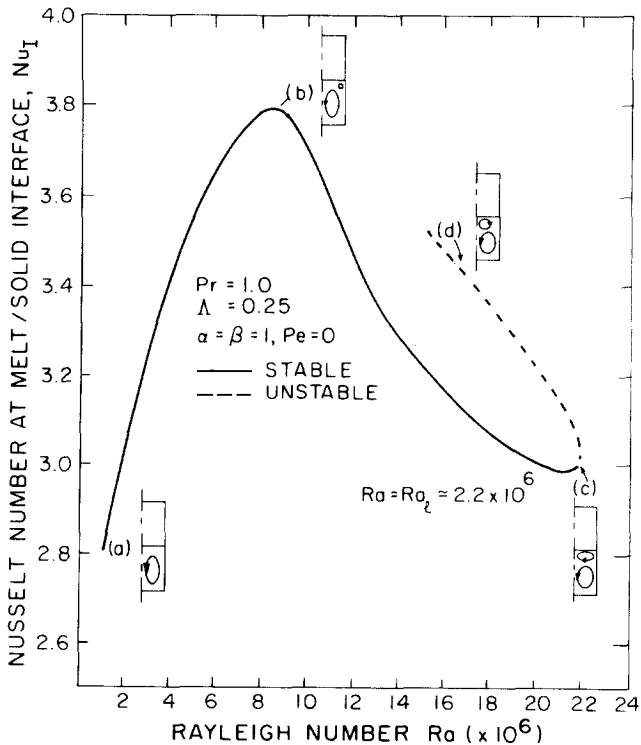

FIG. 12. Families of axisymmetric steady states for the vertical Bridgman system with $\alpha = \beta = 1$, Pe $= 0$, Pr $= 1$, and $\Lambda = 0.25$. Letters refer to sample isotherms and streamlines plotted in Fig. 13.
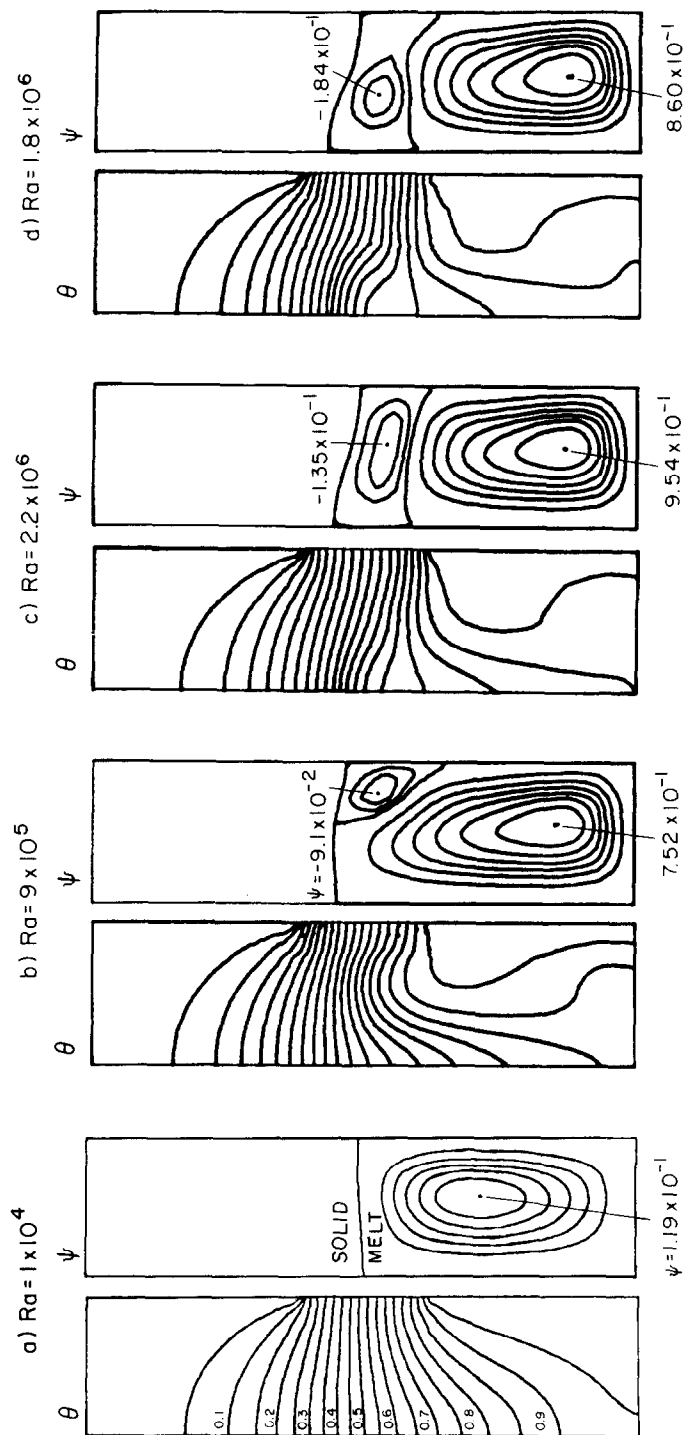
FIG. 13. Representative streamlines and isotherms for vertical Bridgman system with $\alpha = \beta = 1$, $Pe = 0$, $Pr = 1$, and $A = 0.25$. Letters refer to points in Fig. 12.

4.3. *Vertical Bridgman System* $\alpha = \beta = 1$, $Pe = 0$

Adjusting the thermal boundary conditions along the sidewall of the ampoule to fit those of the vertical Bridgman solidification system deformed the axisymmetric flows calculated for the perfect Rayleigh–Bénard problem, but did not appreciably change the structure of the flow family. The family of flows calculated for $\alpha = \beta = 1$ and $Pe = 0$ are represented in Fig. 12 and sample streamlines and isotherms are shown in Fig. 13. The flows at low values of Ra have only a single cell (see Fig. 13a); a second cell formed in the upper corner of the melt (see Fig. 13b) as the Rayleigh number was increased. The second cell spread over the melt–solid interface (see Fig. 13c) and decreased the heat transfer through the surface by masking the interface from the stronger cellular flow.

Just as for the perfect and imperfect Rayleigh–Bénard configurations, a limit point in the family of flows was reached at $Ra = Ra_l^{(1)} \simeq 2.2 \times 10^7$. A new, unstable branch of flows was computed for Rayleigh numbers less than the limiting value Ra_l. In flows along the subcritical branch, the top cell intensified and the bottom cell weakened with decresing Ra, as expected by the similar transition in the imperfect problem between 2U and 1U flow structures. No second limit point was located in the vertical Bridgman calculations in the range $Ra \leqslant 1.4 \times 10^7$, where the 4×16 element mesh was adequate for modelling the flow. Even if one does exist, it is doubtful that the top cell can grow larger than the bottom one and dominate the flow. The discontinuity in thermal boundary condition at the junction of the hot and adiabatic zones drives the bottom cell and most probably constrains the top cell to the adiabatic zone.

5. DISCUSSION

The structure of the steady state flows governed by the Boussinesq equation is complicated. Introducing a deformable melt–solid interface as a phase bounary on the melt does not appreciably change the values of Rayleigh number for the onset of cellular convection, but does alter the "nonlinear" structure of the flow families. The deformation of the interface caused by convective heat transfer destroys symmetry in the flow field that exists for liquid alone in an ampoule, the single-phase problem. This loss of symmetry causes imperfections in secondary bifurcation points that exist for the single-phase problem. The melt–solid interface will generate similar imperfections in families of nonaxisymmetric, fully three-dimensional flows that are known to exist for natural convection in a vertical cylinder. Although the techniques developed here can be directly extended to the analysis of these flows, the calculations are too costly to be undertaken now.

An important observation of this study is the existence of the first limiting value of Rayleigh number Ra_l, beyond which the flow family turns back to lower values of Ra. The calculations presented here and in [12] demonstrate that this limit point is present for the entire sequence of solidification problems, as well as for the single-

phase system. Calculations for any of these systems undertaken without the benefit of the schemes for tracking solution families will no doubt fail to converge near Ra_f and will give no clue to the sudden change in the structure of the flow family at this point. The numerical methods presented here have been used in an extensive study of the flow field and melt–solid interface in the vertically stabilized (melt above crystal) Bridgman system [30].

The changes in the flow structure for the destabilized vertical Bridgman system presented in Subsection 4.3 are simply understood when this configuration is thought of as the limit of a sequence of thermally imperfect solidification problems starting from the perfect two phase Rayleigh–Bénard geometry. Changes in the number of cells in the melt of the Bridgman system result from smooth transitions between flows classified in separate bifurcating families for the perfect Rayleigh–Bénard problem. Understanding the effect of small changes in the thermal boundary conditions on the connectivity of these flow families makes it possible to construct a qualitative picture of the flows in the more complicated system from the numerical results for the perfect problem.

The shape of the melt–solid interface and the flow field are only weakly coupled by convection in the solidification problems studied here. Interface shapes predicted by models for solidification of nondilute alloys [12] and for microscopic instability during solidification [31] are both extremely sensitive to the local composition of the melt and are being studied by the combination of Galerkin finite-element approximations, Newton's method and techniques from bifurcation analysis used here. These methods are equally applicable to other free-boundary problems, such as arise in free-surface fluid mechanics [7, 32] and in the study of confined plasmas [33, 34].

REFERENCES

1. M. C. FLEMING, "Solidification Processing," McGraw-Hill, New York, 1974.
2. T.-W. FU AND W. R. WILCOX, J. Crystal Growth 48 (1980), 416.
3. L.-C. TIEN, Ph. D. thesis, Univ. of Michigan, Ann Arbor, 1968.
4. P. G. KROEGER AND S. OSTRACH, Int. J. Heat Mass Transfer 17 (1974), 1191.
5. H. M. ETTOUNEY AND R. A. BROWN, J. Comput. Phys. 49 (1982), 118.
6. C. J. CHANG AND R. A. BROWN, in "Numerical Properties and Methodologies in Heat Transfer," (T. M. Shih, Ed.), Hemisphere Press, New York, 1983.
7. H. L. SAITÒ AND L. E. SCRIVEN, J. Comput. Phys. 42 (1981), 53.
8. J. M. ORTEGA AND W. E. RHEINBOLDT, "Iterative Solution of Nonlinear Equations in Several Variables," Academic Press, New York, 1970.
9. H. B. KELLER, in "Applications of Bifurcation Theory" (P. H. Rabinowitz, Ed.), Academic Press, New York, 1977.

10. R. A. BROWN, L. E. SCRIVEN, AND W. J. SILLIMAN, in "New Approaches in Nonlinear Dynamics" (P. J. Holmes, Ed.), SIAM, Philadelphia, 1980.
11. Y. YAMAGUCHI, C. J. CHANG, AND R. A. BROWN, Proc. Roy. Soc. London Ser. A, (1983), submitted.
12. R. A. BROWN, C. J. CHANG, AND P. M. ADORNATO, in "Modelling of Casting and Welding Processes," (J. A. Dantzig and J. T. Berry, Eds.), AIME, Warrendale, 1983.
13. G. IOOSS AND D. D. JOSEPH, "Elementary Stability and Bifurcation Theory," Springer-Verlag, New York, 1980.
14. S. CHANDRASEKHAR, "Hydrodynamic and Hydromagnetic Stability," Dover, New York, 1961/1981.
15. G. S. CHARLSON AND R. L. SANI, Int. J. Heat Mass Transfer 13 (1970), 1479.
16. R. E. KELLEY AND D. PAL, in "Proceedings, 1976 Heat Transfer and Fluid Mechanics Institute," Stanford Univ. Press, Stanford, Calif., 1976.
17. P. HALL AND I. C. WALTON, Proc. Roy. Soc. London Ser. A 358 (1977), 199.
18. S. N. BROWN AND K. STEWARTSON, Proc. Roy. Soc. London Ser. A 360 (1978), 455.
19. S. N. BROWN AND K. STEWARTSON, SIAM J. Appl. Math. 36 (1979), 573.
20. J. S. TURNER, "Buoyancy Effects in Fluids," Cambridge Univ. Press, Cambridge, 1973.
21. P. HUYAKORN, C. TAYLOR, R. LEE, AND P. GRESHO, Comput. and Fluids 6 (1978), 25.
22. C. TAYLOR AND A. Z. IJAM, Comput. Math. Appl. Mech. Eng. 19 (1979), 429.
23. G. STRANG AND G. J. FIX, "An Analysis of the Finite Element Method," Prentice–Hall, Englewood Cliffs, N. J., 1973.
24. F. THOMASSET, "Implementation of Finite Element Methods for Navier–Stokes Equations," Springer-Verlag, New York, 1981.
25. C. J. CHANG, Ph. D. thesis, Massachusetts Institute of Technology, Cambridge, Mass., 1982.
26. P. HOOD, Int. J. Num. Meth. Engng. 10 (1976), 379.
27. E. RIKS, J. Appl. Mech. 39 (1972), 1060.
28. L. H. UNGAR AND R. A. BROWN, Philos. Trans. Roy. Soc. London Ser. A 201 (1982), 347.
29. C. J. CHANG AND R. A. BROWN, Int. J. Numer. Meths. Fluids (1983), submitted.
30. C. J. CHANG AND R. A. BROWN, J. Crystal Growth 63 (1983), in press.
31. L. H. UNGAR AND R. A. BROWN, Physical Review B (1983), in press.
32. S. F. KISTLER AND L. E. SCRIVEN, in "Finite Element Flow Analysis" (T. Kawai, Ed.), North-Holland, New York, 1982.
33. D. G. SCHAEFFER, Commun. Partial Differential Equations 2 (1977), 587.
34. J. SIJBRAND, Nonlinear Anal. Theor. Methods Appl. 3 (1979), 723.